CrystEngComm

ROYAL SOCIETY OF CHEMISTRY

PAPER

View Article Online
View Journal | View Issue

Cite this: *CrystEngComm*, 2023, **25**, 6478

In the pursuit of a 'disappearing' anhydrous phase of the antipyrine–dipicolinic acid (ANT–DPA) co-crystal: explained through relative stability and charge density analyses†

Sehrish Akram,[a] Arshad Mehmood, *[b] Sajida Noureen[a] and Maqsood Ahmed *[a]

Received 13th June 2023,
Accepted 28th October 2023

DOI: 10.1039/d3ce00591g

rsc.li/crystengcomm

The relative stability and growth of the two new cocrystal forms of antipyrine–dipicolinic acid, one of which is the 'disappearing' one, were systematically examined. The Cambridge Structural Database was extensively mined to find the hydrogen bonding motifs amenable to crystal engineering. The cocrystallization trials resulted in two cocrystal phases in the same vial. The hydrated phase (**ANT–DPA-w**) is predominant, stable and easily reproducible, while the anhydrous phase (**ANT–DPA**) is the 'disappearing' one which could only be reproduced under anhydrous conditions. The stability of both the cocrystals was examined within the framework of symmetry-adapted perturbation theory (SAPT), non-covalent interactions (NCIs), detailed topological analysis of the electron density and binding energy analyses which provide useful insight into the role of water molecules in the stability of the structure. A thermogravimetric analysis (TGA) was used to identify the dehydration temperature. In light of the above information, the anhydrous phase (**ANT–DPA**) was regained *via* melting and re-crystallization by providing an anhydrous environment to the hydrated phase (**ANT–DPA-w**).

1. Introduction

Crystal engineering involves synthesizing solid-state molecular structures with intermolecular interactions such as hydrogen bonding and coordination bonding.[1] In order to enhance the properties of active pharmaceutical ingredients (APIs), different solid forms are desirable[2] and co-crystallization is one of the best options to achieve that end. A co-crystal consists of two or more molecules that form unique crystalline structures having unique properties. The structural stability of such crystals is usually based upon hydrogen bonding;[3,4] however, other non-covalent interactions such as van der Waals interactions, ionic interactions and π-interactions also play their role.[5] In the co-crystallization, both internal and external factors provide numerous possibilities of supramolecular synthons, resulting in different types of product formation such as co-crystal solvates/hydrates, co-crystal polymorphs or pseudo polymorphs.[6–12] Among solvates, hydrates are the most widely encountered product in small organic drug molecules due to the marvelous potential of water in hydrogen bonding and approximately every third drug molecule can form a hydrate.[13–15] The incorporation of water molecules within the solid state assembly of a drug compound usually affects its pharmaceutical properties such as solubility, dissolution rate, bioavailability, *etc.* by changing its intermolecular interactions.[16–20] The effect of hydrated/anhydrous forms on drug solubility is greater as compared to polymorphism due to the large lattice energy changes observed during hydration.[21,22] Hence, it is very important to identify the hydrated forms in the early phases of pharmaceutical drug development.[23–25] Every compound behaves in a unique way during hydrate formation and hence the conditions of hydrate formation cannot be generalized.[26]

A pharmaceutical co-crystal consists of an API and the co-formers in a stoichiometric ratio.[2,3,27,28] Phenazone (antipyrine) is an active pharmaceutical ingredient with anti-inflammatory and analgesic properties. It was the first pyrazole derivative to be investigated as an antipyretic drug. Due to its toxicity, it is hardly used alone but forms

[a] *Materials Chemistry Laboratory, Institute of Chemistry, The Islamia University of Bahawalpur, Baghdad-ul-Jadeed Campus 63100, Pakistan. E-mail: maqsood.ahmed@iub.edu.pk*

[b] *Institute for Advanced Computational Science, IACS Building, Stony Brook University, Stony Brook, NY 11794, USA. E-mail: arshad.mehmood@stonybrook.edu*

† Electronic supplementary information (ESI) available: Fig. S1 and S2 (TGA/DSC data), S3 and S4 (molecular cluster showing the bond paths) and S5 and S6 (Hirshfeld surface and fingerprint plots). Tables S1 to S8 mention the geometry, Bader's charges and topological parameters. CCDC 2040653–2040683. For ESI and crystallographic data in CIF or other electronic format see DOI: **https://doi.org/10.1039/d3ce00591g**

a combination of products that are used as analgesic drugs.[29] Antipyrine is commonly used as a substrate of the CYP450 enzyme to study the effects of numerous exogenic and endogenic agents as well as drugs on the CYP family.[30] In order to improve the physical properties of various pharmaceutical drugs, di/tricarboxylic acid is systematically introduced as one of the important co-formers.[31] With this concept, we have investigated the cocrystallization of antipyrine (API) with dipicolinic acid (coformer). Dipicolinic acid (DPA) is a chemical compound containing 5 to 15% dry weight of bacterial spores.[32] The low toxicity and amphoteric nature of dipicolinic acid make it more advantageous to enhance the drug's properties.[33–37]

As part of our ongoing curiosity in understanding the crystal engineering of pharmaceutical drugs in terms of electrostatic properties,[38,39] we have been led to new phases of the **ANT–DPA** co-crystal system. The cocrystallization trials resulted in two cocrystal phases in the same vial. The hydrated phase (**ANT–DPA-w**) was predominant, stable, and easily reproducible while the anhydrous phase (**ANT–DPA**) was metastable. It was observed in the same vial as a poor crystal but sufficient enough to allow crystal structure determination. Subsequent trials under different experimental conditions exclusively resulted in **ANT–DPA-w**. These circumstances motivated us to systematically explore as to why the hydrated form remains the probable one and exhibits extra stability. Therefore, the relative stability of both the cocrystals has been examined within the framework of symmetry-adapted perturbation theory (SAPT), non-covalent interactions (NCIs) and binding energy analyses. The topological analysis employing Bader's quantum theory of atoms in molecules (QTAIM)[40,41] serves as an indispensable tool for discerning non-covalent interactions within crystals. This method unveils critical points and bond paths that define these intermolecular forces. Our goal was to use a whole range of theoretical and experimental methods to ascertain the relative stability of both the cocrystals with an aim to find the 'lost' phase. The results obtained furnished valuable insights and paved the way for regaining the 'disappearing' anhydrous phase **ANT–DPA** (Scheme 1).

2. Experimental

2.1. Materials

Antipyrine (1,2-dihydro-1,5-dimethyl-2-phenyl-3*H*-pyrazol-3-one) and dipicolinic acid (pyridine-2,6-dicarboxylic acid) were received from Sigma-Aldrich and used without further purification.

2.2. Growth of co-crystals

For the synthesis of the **ANT–DPA** co-crystal, antipyrine and dipicolinic acid in an equal stoichiometric ratio were dissolved in 20 ml ethanol. The solution was refluxed at 50 °C for two hours. After refluxing, the solution was transferred into a crystallization vial and the solvent was allowed to evaporate at room temperature. Colorless block-shaped crystals were harvested within 5 days. Crystal screening showed the hydrated cocrystal (**ANT–DPA-w**) in the bulk form; however, the anhydrous phase (**ANT–DPA**) was found serendipitously during a routine screening in the same vial as a poorly diffracting weak crystal. Repeated crystallization trials under varying conditions were conducted to obtain better quality crystals of **ANT–DPA**. However, it always resulted in the hydrated phase (**ANT–DPA-w**) as the reproducible and stable phase. Extensive computational and thermal analyses, described in the coming sections, were undertaken to find the 'disappearing' phase (**ANT–DPA**). The results indicated that the presence of water dictates the predominance of **ANT–DPA-w**. **ANT–DPA** could ultimately be obtained from the melt under an anhydrous environment, as detailed below. Table 1 gives the crystallographic and refinement details of both the cocrystals.

2.3. Thermal analysis (TGA/DSC) and melt co-crystallization

In order to examine the thermal behavior of the hydrated co-crystal (**ANT–DPA-w**), TGA/DSC analysis was conducted on a Perkin Elmer STA 6000 up to 500 °C. A measured amount of the sample was used in a ceramic crucible and was heated at a rate of 20 °C min^{-1} from 30 °C to 500 °C as shown in Fig. S1a.† Nitrogen was used as the purge gas at 20 ml min^{-1}. The data analysis shows that the co-crystal remains stable up to 200 °C, with a small weight loss (5%). An endothermic peak

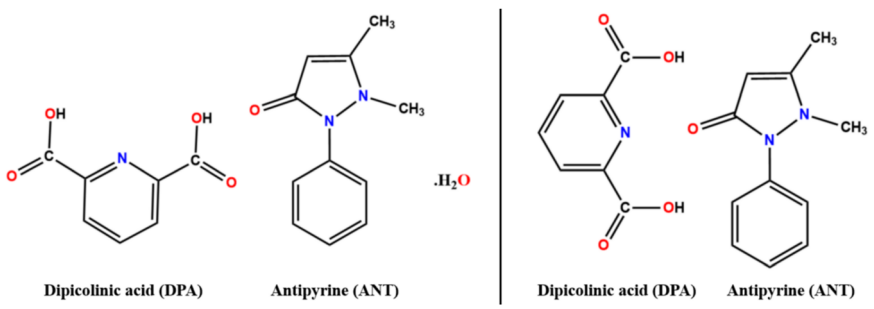

Scheme 1 Chemical structures of pharmaceutical co-crystals, (I) **ANT–DPA-w** cocrystal (hydrated) and (II) **ANT–DPA** co-crystal (anhydrous).

Table 1 Crystallographic and refinement details

Crystal data	ANT–DPA-w	ANT–DPA
Chemical formula	$C_{18}H_{17}N_3O_5{\cdot}H_2O$	$C_{18}H_{17}N_3O_5$
M_r	373.37	355.34
Crystal system, space group	Monoclinic, $C2/c$	Orthorhombic, $Aea2$
Temperature (K)	100(2)	100(2)
a, b, c (Å)	18.4087(1), 8.0394(7), 23.690(2)	36.6912(1), 13.4523(6), 6.6207(3)
β	91.284(4)	
V (Å^3)	3505.1(1)	3267.9(2)
Z	8	8
Radiation type	Mo Kα	Mo Kα
μ (mm^{-1})	0.11	0.11
Crystal size (mm)	0.28 × 0.178 × 0.12	0.076 × 0.130 × 0.158
Data collection		
Diffractometer	Bruker D8 Venture PHOTON II	Bruker D8 Venture PHOTON II
Absorption correction	Multi-scan	Numerical
No. of measured, independent and absorbed reflections	50 750, 5845, 4909	11 879, 4155, 3790
R_{int}	0.068	0.031
$\sin\theta/\lambda_{max}$ (Å^{-1})	0.735	0.667
Refinement		
$R[F^2 > 2\sigma(F^2)]$	0.059	0.036
w$R(F^2)$	0.159	0.084
S	1.05	1.05
No. of parameters	262	243
H-atom treatment	H atom treated by a mixture of independent and constrained refinement	H atom treated by a mixture of independent and constrained refinement
$\Delta\rho_{max}$, $\Delta\rho_{min}$ (e Å^{-3})	0.59, −0.37	0.22, −0.19

appears at 101 °C as shown in Fig. S1a and S2a,† indicating the removal of water molecules from **ANT–DPA-w**. The binding strength of water molecules in **ANT–DPA-w** was estimated by calculating the vaporization enthalpy (ΔH_s = 15 kcal mol^{-1}) of the cocrystal-bound solvent by using the following relationship[42]

$$\Delta H_s = (\Delta H^T_{dehyd} \times 100/\Delta m_s) \times M_s$$

(ΔH^T_{dehyd} = dehydration enthalpy, Δm_s = mass loss percent, M_s = molecular weight of solvent)

The information obtained from the data was used to reproduce **ANT–DPA** from **ANT–DPA-w** by melt co-crystallization. For this purpose, the latter was heated up to 150 °C which is well above the dehydration temperature (≈101 °C) but below the degradation temperature (≈200 °C). In order to keep the environment anhydrous, 10 ml analytical grade dichloromethane was instantaneously added to the melt. After a few days, a needle-shaped colorless co-crystal was obtained which proved to be **ANT–DPA** upon screening by single crystal diffraction. The TGA/DSC analysis also shows the absence of water molecules in the crystal structure with no weight loss at 101 °C as shown in Fig. S1b and S2b.†

2.4. Single crystal X-ray diffraction (SCXRD)

Single crystals of both the cocrystals were chosen under an Olympus ZX10 polarizing microscope, placed on a glass needle with the help of inert grease and mounted on the goniometer head of an X-ray diffractometer. The single crystal X-ray diffraction data of both cocrystals were collected on a Bruker D8 Venture with PHOTON II Detector single crystal X-ray diffractometer using Mo Kα radiation (λ = 0.71073 Å) at 100 K using an Oxford Cobra Cryosystem. The data integration and reduction were performed with SAINT[43] software, and the empirical absorption correction was performed using the SADABS[43] program.

2.5. Structure solution and refinement

The crystal structure of **ANT–DPA-w** was solved in the space group $C2/c$, while that of **ANT–DPA** was solved in the orthorhombic crystal system with the space group $Aea2$ by direct methods using the Olex2 software.[44] All of the H atoms were located in the difference Fourier maps. The riding model[45] was used for the H atoms bonded to C atoms while the H atoms attached to the heteroatoms were refined freely.

The crystal data and structural refinement details of both cocrystals are summarized in Table 1.

2.6. Computational details

The density functional theory (DFT) based theoretical calculations on both the cocrystals were carried out in three stages. In the first stage, a full periodic geometry optimization including coordinates and cells was performed using the CRYSTAL17 (ref. 46) suite of programs, starting with the geometries obtained from the refined and validated crystal structure. The optimization used ωB97X,[47] a long-range corrected density functional, and pob-TZVP-rev2 (ref. 48) basis sets. The shrinking factors (IS1, IS2, and IS3) along with the reciprocal lattice vectors were set to 8, corresponding to 150 k points in the irreducible Brillouin zone. The bielectronic Coulomb and exchange series values for the truncation parameter (ITOL$_i$, for i = 1–4) were set to 9 and ITOL$_5$ to 30, while the eigenvalue level shifter was set to 1.0 Hartree and maintained after diagonalization. The percent of Fock/KS matrix mixing was set to 20 and the default extra-large integration grid and convergence criteria were adopted during the calculations. The converged periodic wave functions were used to perform the Bader charge analysis using the TOPOND suite interfaced with CRYSTAL17.[49,50]

In the second stage, the coordinates of asymmetric units were extracted from the unit cells optimized in the first stage. Gas phase single point calculations on both cocrystals were carried out using the Gaussian 16 (ref. 51) suite of programs at the M062X[52]/aug-cc-pVDZ[53] level. The corrections for basis set superposition error and dispersion interactions were invoked by using the Boys–Bernardi counterpoise method[54] and Grimme's D3 methods, respectively, as implemented in Gaussian16. The obtained wavefunction was used to perform the non-covalent interaction (NCI)[55] analysis and to calculate

the other properties using the Multiwfn analysis program.[56] The same level of theory was used to optimize the geometries and to calculate the vibrational frequencies of isolated molecules in the gas phase. The non-covalent interactions were further analyzed within the framework of symmetry-adapted perturbation theory (SAPT)[57,58] by using the PS14 (ref. 59) program. The optimized coordinates of asymmetric units were used for SAPT analysis using the aug-cc-pVDZ basis set.

During the third stage of the study, single-point energy calculations were conducted within the crystalline phase, utilizing experimental coordinates with CRYSTAL17. The resulting wavefunction served as input for the topological analysis of electron density, which was performed using the TOPOND suite. To identify critical points within the electron density, a global search strategy was used restricting the analysis to a maximum of seven neighboring atoms in the nearest neighbor analysis around each unique critical point. Furthermore, a maximum cluster radius of 7 Å was imposed. In particular, we focused on evaluating the bond (3,–1) critical points involving non-bonded atoms in order to quantitatively assess non-covalent interactions.

3. Results and discussion

3.1. Crystal structure analysis

The hydrated co-crystal (**ANT–DPA-w**) crystallizes in the space group $C2/c$ with lattice dimensions of a = 18.4087(1) Å, b = 8.0394(7) Å, c = 23.690(2) Å and V = 3505.1(1) Å^3. The asymmetric unit consists of one molecule each of antipyrine, dipicolinic acid, and water. The anhydrous co-crystal (**ANT–DPA**) belongs to the orthorhombic $Aea2$ space group with lattice dimensions of a = 36.6912(1) Å, b = 13.4523(6) Å, c = 6.6207(3) Å and V = 3267.9(2) Å^3. The asymmetric unit consists of one molecule of dipicolinic acid and one molecule of antipyrine as shown in Fig. 1.

In **ANT–DPA-w**, the dihedral angle between the mean plane C12 C14 C16 of the dipicolinic acid and the mean plane C7 C9 N1 of the pyrazolone ring is 16°(1); however, the dihedral angle between the mean plane C1 C3 C5 of the phenyl ring of antipyrine and the dipicolinic acid is 55.70°(1). The phenyl torsion angle of the atoms C6–C1–N1–C9 is −52.60°(2). The structural analysis revealed that the molecular assembly in **ANT–DPA-w** is stabilized by strong hydrogen bonding including O–H_{DPA}···O_{ANT} (2.438(17) Å) between the carboxylic group of dipicolinic acid and the oxygen of antipyrine as well as O–H_{DPA}···O_W (2.659(17) Å), O–H_W···O_{DPA} (2.877(17) Å), and O–H_W···N_{DPA} (2.906(18) Å) hydrogen bonding of the carboxylic group and nitrogen of the dipicolinic acid with a water molecule to form a ring synthon. The oxygen of the carboxyl group in dipicolinic acid is more electronegative and is a good acceptor of the hydrogen atom of water molecules as compared to nitrogen. So, these two –COOH functional groups of dipicolinic acid are connected to two water molecules by O–H_{DPA}···O_W and O–H_W···O_{DPA} and result in the formation of ring synthon $R_2^2(8)$ by providing additional stability to **ANT–DPA-w** through hydrogen bonding. These hydrogen bonds form a closed association between two dipicolinic acid molecules, two water molecules and two antipyrine molecules Fig. 2. On the other hand, in the **ANT–DPA** form, the dihedral angle between the mean plane C12 C14 C16 of the dipicolinic acid and the mean plane C7 C9 N1 of the pyrazolone ring is 3.50°(1) and the phenyl torsion angle of the atoms C6–C1–N1–C9 is −114.82°(2). This happens due to the appearance of both bulky groups (–COOH) of dipicolinic acid towards the oxygen of antipyrine. Unlike **ANT–DPA-w**, due to the absence of water molecules it forms only one synthon between dipicolinic acid and antipyrine molecules. The oxygen of antipyrine acts as a hydrogen atom acceptor of both carboxylic groups of dipicolinic acid to form hydrogen bonds *via* two O–H_{DPA}···O_{ANT} (2.672(2) Å;

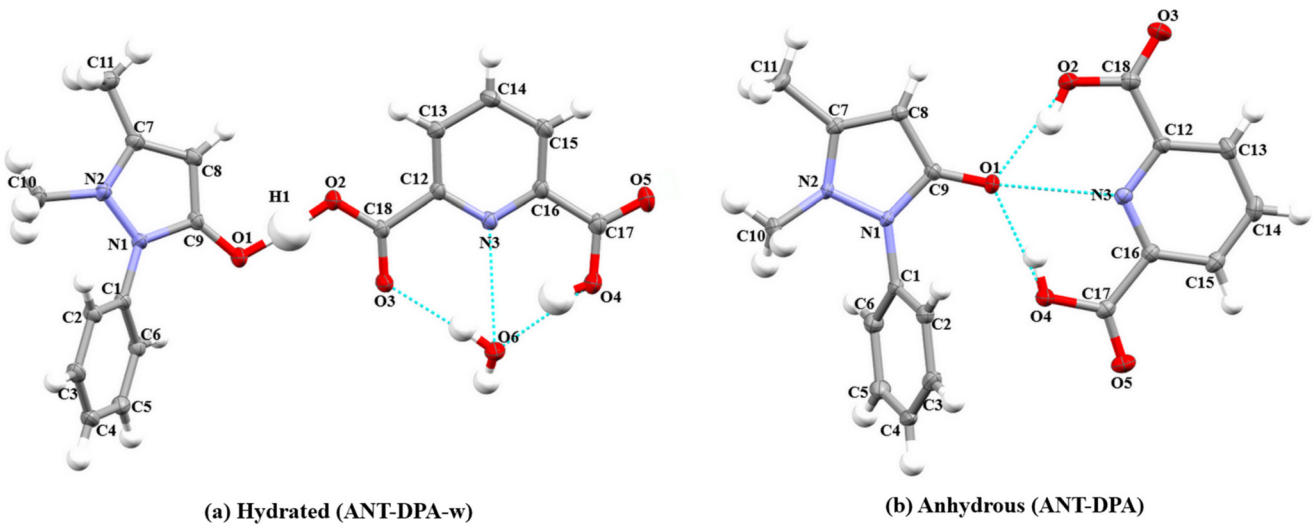

Fig. 1 Thermal ellipsoid plots (@50% probability) of the asymmetric units of (a) hydrated (ANT–DPA-w) and (b) anhydrous (ANT–DPA) co-crystals showing the atom numbering scheme for non-H atoms.

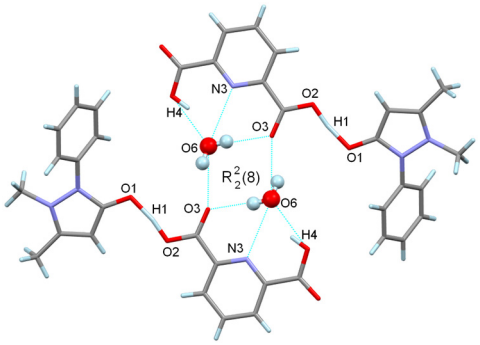

Fig. 2 Ring motif in **ANT–DPA-w**, showing the role of water in the cocrystal assembly.

2.681(2) Å) hydrogen bonds as well as to form weak intermolecular interaction with the nitrogen of dipicolinic acid C–O_{ANT}···N_{DPA} (4.103(2) Å) as shown in Fig. 1.

In the packing of **ANT–DPA-w**, the water molecule plays a significant role in stabilizing the co-crystal assemblies by interacting *via* weak and strong intermolecular interactions between the asymmetric units to form stacks and form inclined parallel layers along the crystallographic *b* axes (Fig. 3a). The weak interactions which stabilize the packing include C4–H4A···O5^{i} (3.348(2) Å), C10–H10C···C5^{ii} (3.423(3) Å), C3–H3···N3^{v} (3.328(2) Å) and C6–H6···C14^{vi} (3.564(3) Å). In the case of **ANT–DPA**, the unit cell was arranged in parallel layers along the *b* axes (Fig. 3b), *via* strong as well as weak interactions including C14–H14···O3^{ii} (3.472(3) Å) and C6–H6···O5^{v} (3.215(3) Å) [symmetry codes same as in Table 3]. Hirshfeld surface[60,61] and 'fingerprint' analyses for the asymmetric unit of both the cocrystals were mapped with d_{norm} separately using CrystalExplorer17 (ref. 62) and are shown in Fig. S5 and S6.† This analysis indicates that the surface is predominated by O···H interactions whose contribution is highest in water followed by dipicolinic acid and antipyrine moieties in **ANT–DPA-w** and **ANT–DPA**, respectively.

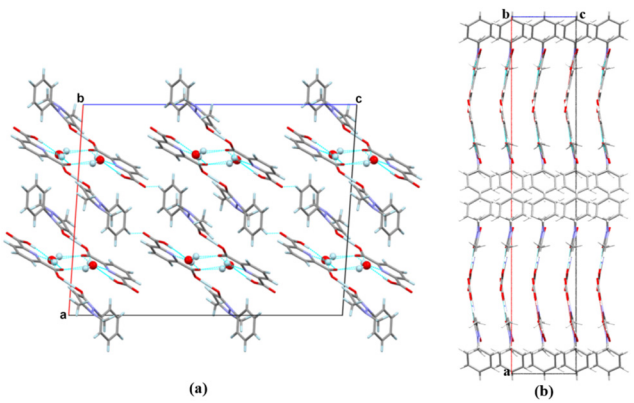

Fig. 3 A view of molecular packing along the *b* axis: (a) **ANT–DPA-w** and (b) **ANT–DPA**.

3.2. Computational insights

The comparison between the experimental and DFT optimized geometries of both the cocrystals using periodic boundary conditions is provided in the ESI.† Similarly, Table S1† compares the experimental and optimized lattice parameters. For both the cocrystals, the experimental and optimized geometries are comparable, and the most significant differences can be observed in the relative positions of methyl hydrogens in the pyrazole ring. These small differences in the hydrogen positions can be attributed to the lack of high-resolution diffraction data, required to locate the hydrogen positions precisely or due to the reorientation of methyl groups upon energy minimization in DFT calculations. Generally, H atoms are omitted during the comparisons between experiment and theory.[63] For **ANT–DPA-w**, the significant differences in the lattice parameters are shown by length *c* which is decreased by about 2% in the DFT optimized structure followed by a ~1.9% reduction in angle *β*. For **ANT–DPA**, the largest difference can be noticed for length *a* which is reduced by ~3.4% in the optimized unit cell. A relative comparison of unit-cell volumes shows that for **ANT–DPA-w**, the volume is reduced by 2.4% upon optimization, whereas for **ANT–DPA** the difference is much more significant and a reduction of 10.5% is noticed. These differences are due to the absence of thermal corrections in DFT calculations where the systematic error in the lattice constants scale cubically for the volume. This major difference for **ANT–DPA** is not unique, as a reduction as large as 6.96% and 8.44% has been reported even for smaller unit cells such as ammonia and benzene, respectively.[64] Overall, our DFT optimization validates the experimental structures of both the cocrystals.

The binding energies computed using the relation: $\Delta E_{A-B} = E_{AB} - E_A - E_B$ and $\Delta E_{A-B-C} = E_{ABC} - E_A - E_B - E_C$ respectively for the dimeric pairs and trimeric combination for both the cocrystals are given in Table 2 along with the solid-state Bader charge transfer and results of SAPT analysis. For **ANT–DPA-w**, the interaction energies reveal that antipyrine (A) and the combination of dipicolinic acid (B) and water (C) form the most stable pair due to the strong O–H···O interactions, and energetically, this pair is the significant contributor in

Table 2 Binding energies, ΔE (kcal mol^{-1}), charge transfer, CT (e), and results of SAPT0 analysis, expressed in kcal mol^{-1} with decomposed non-covalent interaction energies as E_L: electrostatic, E_X: exchange, *I*: induction, and *D*: dispersion components

	ANT–DPA-w			**ANT–DPA**
Constituent	A···BC	AB···C	A···B···C	A···B
ΔE	−27.19	−18.87	−43.62	−29.67
CT	0.125	−0.013	—	0.0736
E_{SAPT0}	−29.69	−20.45	—	−35.33
E_L	−40.88	−31.42	—	−45.53
E_X	53.22	34.14	—	47.87
I	−32.53	−14.95	—	−21.90
D	−9.503	−8.217	—	−15.77

the trimer formation. This interaction is similar in strength to that in **ANT–DPA**, and the different orientation of A and B in **ANT–DPA** provides additional stability by ~2.5 kcal mol^{-1}. This additional stability is due to the involvement of an added O–H···O interaction which bifurcates the H-bonding interactions of antipyrine oxygen. Table 2 further reveals that the interaction between water (C) and a combination of antipyrine (A) and dipicolinic acid (B) in **ANT–DPA-w** provides a stability of ~19 kcal mol^{-1}, which is absent in **ANT–DPA**. This value is in close agreement with the experimentally measured enthalpy of dehydration (ΔH_s = 15 kcal mol^{-1}) as discussed in section 2.3. Though the binding of A with B in **ANT–DPA-w** is weaker compared to that in **ANT–DPA**, the stronger interactions of solvents in **ANT–DPA-w** impart higher stabilization to the trimer. For both the cocrystals, the computed binding energies with and without counterpoise corrections (not shown) follow the same trend and show significant cooperativity-induced stabilization from both hydrogen bonding in co-formers and solvent molecules. Nevertheless, the interaction between A and B in both the cocrystals plays the dominant role in bestowing stability to the trimer and dimer, respectively.

The charge transfer calculated from the Bader charge analysis on the electron density obtained from periodic DFT calculations are given in Table 2. The calculated Bader charges on each constituent atom of both the cocrystals are given in ESI† Table S2. Although the charge-based quantum mechanical exploration of intermolecular interactions is a rather complex issue, in the present study, the charge transfer between components is quite consistent with binding energies, and thus, can be considered as reliable. As expected, the oxygen of antipyrine in **ANT–DPA-w** is the most electron-rich atom of the moiety followed by N1 and N2 carrying −1.2e, −0.82e, and −0.80e charges, respectively. Similarly, the carbonyl carbon C9 in antipyrine is the most electron-depleted atom having a charge of 1.2e. In the B component of **ANT–DPA-w**, all the oxygen atoms are the most negatively charged atoms whereas the carboxylic carbons C17 and C18 are the most positively charged atoms of the moiety. The N3 nitrogen atom of B is less negatively charged while the carboxylic groups of the B component are considerably polarized. Exactly, similar trends can be noticed for the components of **ANT–DPA**. However, it is important to note that the sum of charges on all atoms of component A in **ANT–DPA-w** is more positive than that in **ANT–DPA**, and the sum of charges on all atoms of component B in **ANT–DPA-w** is more negative than that in **ANT–DPA**, indicating that the components of **ANT–DPA-w** are more polarized compared to those of **ANT–DPA**. This enhanced contribution of electrostatics in **ANT–DPA-w** is consistent with its large binding energies relative to **ANT–DPA**. As shown in Table 2, a net charge transfer of 0.125e takes place from A to BC in **ANT–DPA-w**, while this charge transfer is relatively smaller between A and B in **ANT–DPA**. In addition, a net charge of 0.013e transfers from C to AB in **ANT–DPA-w**. These observations suggest that the charge transfer between water to other components in **ANT–DPA-w** is a significant contributor to its higher binding energy, relative to **ANT–DPA**.

In order to further explain the difference in binding energies of both the cocrystals, we used SAPT0 analysis which decomposes the non-covalent interaction energy into four components, electrostatic (E_L), exchange (E_X), induction (I), and dispersion (D). The first component, E_L, mainly originates from Coulombic multipole–multipole interactions between the interacting monomers. The second component E_X represents the repulsive interactions imparted by the spatial overlap of monomer wave functions in combination with dimer wave function after an exchange of electronic coordinates. The induction component, I, results from the polarization induced by the responses of monomers to each other's electric field in combination with the charge transfer between the monomers. The last component, D, represents the attractive interaction originating from the dynamical correlation between electrons on one monomer and those on the other.[57] Table 2 provides the values of these components for both the cocrystals, including total SAPT0 interaction energies. The E_{SAPT0} complements the binding energies by showing that the solvent component (C) imparts additional stability (−20.45 kcal mol^{-1}) to the complex in **ANT–DPA-w** again being in close agreement with the experimentally measured ($\Delta_{Dehydration}$ = 15 kcal mol^{-1}). If the contribution of water is eliminated, **ANT–DPA** becomes more stable (~6 kcal mol^{-1}) compared to **ANT–DPA-w**. Among the attractive components, the E_L is principally responsible for holding the components together in both the cocrystals, signifying the role of electrostatic interactions. It is important to note that repulsive forces due to the E_X are higher than any of the individual attractive components. However, these forces are compensated by the combination of stronger attractive forces mainly E_L and I. The D component has nearly similar values for A···BC and AB···C in **ANT–DPA-w**; however, its significantly larger value for **ANT–DPA** represents the involvement of additional dispersion interactions due to the change in orientation.

To further visualize these interactions in real space, we performed the noncovalent interaction (NCI)[65] analysis which is also known as the reduced density gradient (RDG) method. The NCI provides a robust way to visualize the weak interactions including the van der Waals (vdW) and dispersion interactions. The top of Fig. 4(a) presents the plots of RGD plotted against the sign(λ_2)ρ for **ANT–DPA-w** while the bottom figure shows the various types of interactions in the real space. The location of bond critical points and intramolecular bond paths are also included in the bottom figure to better elaborate the location of sign(λ_2)ρ. Most interactions between the A and B components of **ANT–DPA-w** are mainly vdW types of interactions as revealed by the dominant green color in the bottom figure and spikes located around zero in the top figure. The strongest attractive

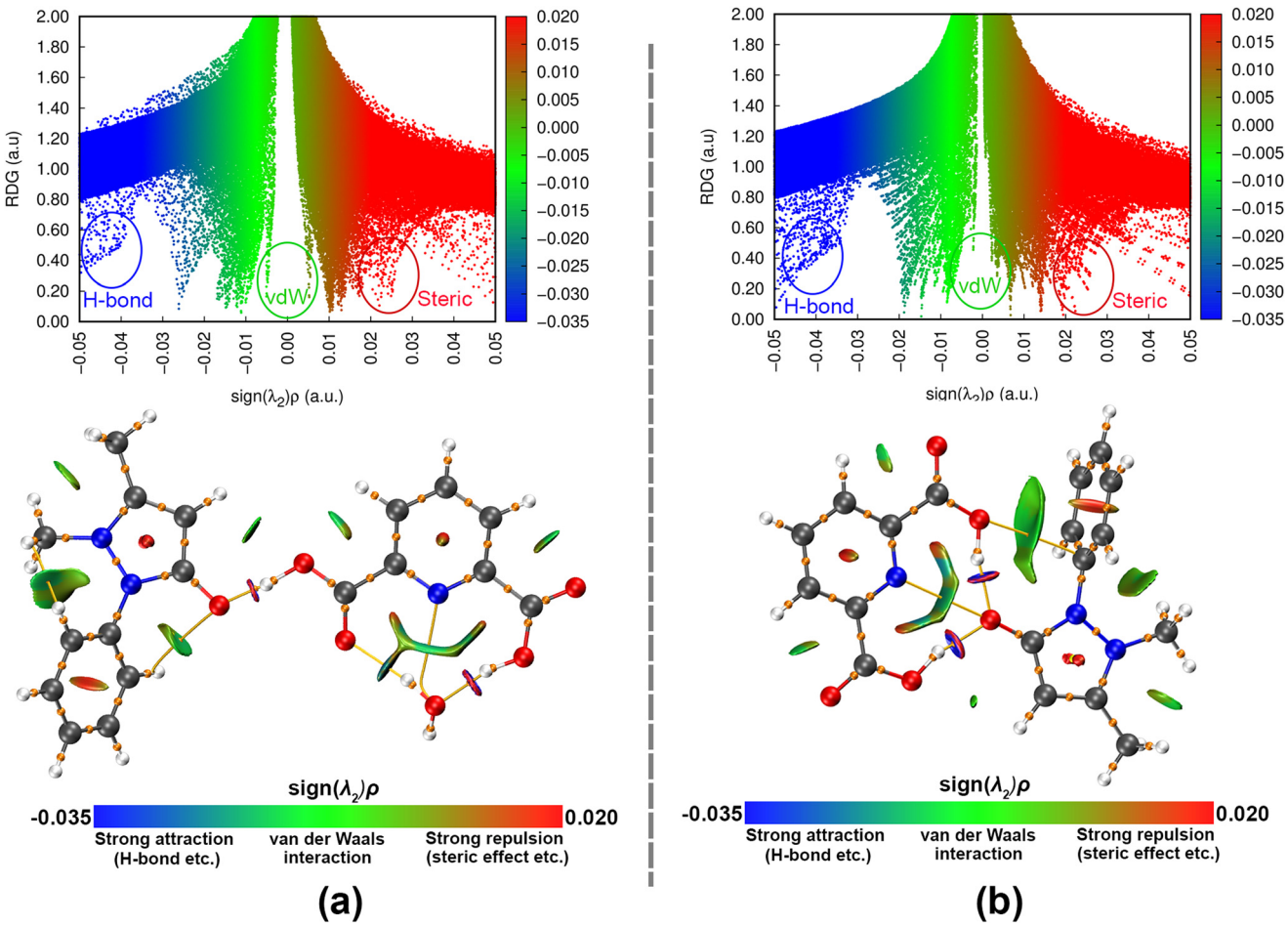

Fig. 4 (a and b): NCI colored scatter graphs (top) and RDG isosurface plots (bottom) for both cocrystals (a) **ANT–DPA-w** and (b) **ANT–DPA**. The various types of interaction regions are marked by colored circles. The orange dots on bonds and orange line between atoms represent the location of bond critical points and intramolecular bond paths, respectively.

interaction is the hydrogen bonding O–H···O, present between the carbonyl oxygen of A and carboxylic oxygen of B. The water molecule (C) forms a variety of interactions between various atoms of B, including N3, O3, and O4. It is important to note that though water is important for providing additional stability as mentioned above and for unit cell packing, the significant role in dimer formation is only played by the hydrogen bonding interaction between the major components A and B of **ANT–DPA-w**. Fig. 4(b) shows similar NCI plots for **ANT–DPA** and exhibits a nearly similar behavior between the components of **ANT–DPA**. In contrast to **ANT–DPA-w**, the components of **ANT–DPA** contain a variety of van der Waals (vdW) interactions between π-electrons of A and one carboxylic group of B, which explains the higher values of the dispersion component in SAPT0 analysis given in Table 2. The relative comparison of SAPT0, NCI, and binding energy analysis for both systems suggests that the higher binding energy of **ANT–DPA-w** is due to the stability imparted by the H-bonding of water molecules. From these theoretical studies, it can be inferred that the presence of a variety of intermolecular forces, mainly H-bonding between the constituent molecules, leads to co-crystal formation.

3.3. Topological analysis of intermolecular properties

To assess the non-covalent interactions within the ANT, DPA, and water molecules, we conducted a topological analysis of the electron density. This analysis was performed using the TOPOND suite, utilizing experimental coordinates. Tables 3 and 4 list the topological parameters of non-covalent interactions in both the cocrystals. Most of the interactions follow the first four of Koch and Popelier's criteria[66] for the formation of hydrogen bonds in the crystal system. Topological analysis of intermolecular interactions reveals that both the cocrystals are stabilized by strong O···H–O hydrogen bonds with a large value of electron density at the critical point and a large value of potential as well as kinetic energy. In **ANT–DPA-w**, the hydrogen bond O1···H1–O2 between antipyrine and dipicolinic acid is stronger with an electron density on the critical point of ρ = 0.830 e Å^{-3} as well as a higher potential energy = −403 kJ mol^{-1} Bohr^{-3}. However, the hydrogen bonds O6···H4–O4 (ρ = 0.35 e Å^{-3}, potential energy = −146 kJ mol^{-1} Bohr^{-3}) and O3···H6a–O6 (ρ = 0.1751 e Å^{-3}, potential energy = −60.07 kJ mol^{-1} Bohr^{-3}) between dipicolinic acid and a water molecule is weaker as compared

Table 3 Topological properties of (3,–1) CPs in the intermolecular interactions of the hydrated form: distances (Å), electron density (e Å^{-3}), Laplacian (e Å^{-5}), Hessian eigenvalues (e Å^{-5}), ε = ellipticity, G_{CP} = bond kinetic-energy density (kJ mol^{-1} Bohr^{-3}) and V_{CP} = bond potential-energy density (kJ mol^{-1} Bohr^{-3})

No.	Bonds	d_{12}	d_{1CP}	d_{2CP}	$\rho_{BCP}(r)$	$\nabla^2\rho_{BCP}(r)$	λ_1	λ_2	λ_3	ε	G_{CP}	V_{CP}
1	O2–H1⋯O1	1.314	0.351	0.963	0.83	0.940	−8.097	−7.856	16.89	0.028	214.2	−403.0
2	O4–H4⋯O6	1.646	0.524	1.122	0.351	3.109	−2.338	−2.241	7.687	0.04	115.3	−146.0
3	O6–H6a⋯O3^{iv}	1.898	0.669	1.229	0.175	2.458	−0.892	−0.868	4.241	0.034	63.61	−60.07
4	O6–H6b⋯O3	1.91	0.659	1.251	0.175	2.362	−0.94	−0.916	4.217	0.026	62.61	−60.90
5	C3–H3⋯N3^{v}	2.384	0.934	1.45	0.081	1.036	−0.289	−0.241	1.566	0.115	23.83	−19.33
6	C4–H4a⋯O5^{i}	2.351	0.923	1.428	0.074	1.060	−0.265	−0.265	1.615	0.012	23.06	−16.95
7	C10–H10c⋯C5^{ii}	2.443	0.948	1.495	0.074	0.892	−0.241	−0.145	1.253	0.658	20.01	−15.81
8	C11–H11c⋯O3^{ii}	2.533	1.019	1.514	0.054	0.699	−0.169	−0.145	1.012	0.081	14.67	−10.63
9	C6–H6⋯C14^{vi}	2.648	1.061	1.587	0.054	0.578	−0.145	−0.096	0.819	0.774	13.32	−10.81
10	C3–H3⋯O6^{v}	2.658	1.126	1.532	0.047	0.602	−0.096	−0.096	0.819	0.071	13.38	−10.03
11	C15–H15⋯C3^{iii}	2.701	1.091	1.61	0.047	0.506	−0.12	−0.096	0.723	0.209	11.78	−9.75
12	C5–H5⋯O4	2.741	1.165	1.576	0.04	0.506	−0.096	−0.072	0.699	0.248	10.99	−8.383
13	C5–H5⋯O5	2.659	1.049	1.61	0.04	0.506	−0.12	−0.096	0.723	0.115	10.43	−7.162
14	C10–H10a⋯O5	2.683	1.158	1.525	0.04	0.554	−0.12	−0.12	0.795	0.044	12.44	−9.575
15	C11–H11a⋯O1	2.868	1.251	1.617	0.034	0.410	−0.096	−0.072	0.554	0.293	9.108	−7.209
16	C8–H8⋯O6	2.727	1.072	1.655	0.034	0.434	−0.096	−0.072	0.602	0.31	8.874	−5.9
17	C2–H2⋯O6	2.835	1.199	1.636	0.034	0.434	−0.096	−0.072	0.602	0.237	9.797	−7.55
18	C11–H11a⋯O4	2.842	1.217	1.625	0.034	0.386	−0.072	−0.072	0.53	0.212	8.507	−6.25

Symmetry codes: (i) $x - 1/2, -y + 1/2, z - 1/2$; (ii) $x, y + 1, z$; (iii) $x + 1/2, -y + 3/2, z + 1/2$; (iv) $-x + 3/2, -y + 1/2, -z + 1$; (v) $-x + 1, -y + 1, -z + 1$; (vi) $-x + 3/2, -y + 3/2, -z + 1$.

Table 4 Topological properties of (3,–1) CPs in the intermolecular interactions of the anhydrous form. Experimental values (above) and theoretical values (below): distances (Å), electron density (e Å^{-3}), Laplacian (e Å^{-5}), Hessian eigenvalues (e Å^{-5}), ε = ellipticity, G_{CP} = bond kinetic-energy density (kJ mol^{-1} Bohr^{-3}) and V_{CP} = bond potential-energy density (kJ mol^{-1} Bohr^{-3})

No.	Bonds	d_{12}	d_{1CP}	d_{2CP}	$\rho_{BCP}(r)$	$\nabla^2\rho_{BCP}(r)$	λ_1	λ_2	λ_3	ε	G_{CP}	V_{CP}
1	O4–H4A⋯O1	1.657	0.533	1.124	0.331	3.157	−2.121	−2.072	7.374	0.026	112.2	−138.1
2	O2–H2A⋯O1	1.692	0.55	1.142	0.304	3.061	−1.928	−1.88	6.844	0.028	103.9	−124.7
3	C6–H6⋯O5^{v}	2.204	0.866	1.338	0.094	1.494	−0.361	−0.337	2.169	0.065	32.32	−24.26
4	C11–H11C⋯O3^{iv}	2.229	0.87	1.359	0.088	1.325	−0.313	−0.289	1.952	0.086	27.95	−19.88
5	C14–H14⋯O3^{ii}	2.38	0.904	1.476	0.067	0.988	−0.241	−0.241	1.47	0.025	20.49	−14.21
6	C15–H15⋯C11^{i}	2.617	1.04	1.577	0.054	0.699	−0.12	−0.048	0.868	1.43	15.05	−11.39
7	C4–H4⋯O5	2.655	1.085	1.57	0.047	0.554	−0.145	−0.12	0.819	0.047	11.93	−9.021
8	C11–H11A⋯O4	2.731	1.126	1.605	0.04	0.506	−0.12	−0.072	0.699	0.416	11.09	−8.16
9	C8–H8⋯O3	2.87	1.198	1.672	0.027	0.361	−0.072	−0.048	0.482	0.455	7.639	−5.732

Symmetry codes: (i) $x, y - 1, z$; (ii) $-x + 1/2, y - 1/2, z$; (iii) $x, y + 1/2, z - 1/2$; (iv) $-x + 1/2, y + 1/2, z$; (v) $x, y + 1/2, z + 1/2$.

to the O1⋯H1–O2 hydrogen bond. In **ANT–DPA**, due to the absence of water molecules, both the carboxylic groups of dipicolinic acid form a hydrogen bond with antipyrine and the crystal geometry is stabilized by two O⋯H–O hydrogen bonds including O1⋯H4A–O4 (ρ = 0.331 e Å^{-3}, potential energy = −138.1 kJ mol^{-1} Bohr^{-3}) and O1⋯H2A–O2 (ρ = 0.304 e Å^{-3}, potential energy = −124.7 kJ mol^{-1} Bohr^{-3}). From the above discussion, we conclude that in the presence of water molecules in **ANT–DPA**, **ANT–DPA-w** is the most stable conformation and after the removal of water molecules, **ANT–DPA** is more stable.

3.4. Electrostatic potential and electrostatic interaction energies

The electrostatic potential is a physically observable quantity developed by electrons and a system of nuclei by using Coulomb's law.[67,68] It provides qualitative as well as quantitative information about the chemical reactivity of the molecular structure and its binding ability with its neighboring molecule in the biological environment.[69–73] The region of positive potential is predicted to be the electrophilic sites while the negative potential shows the nucleophilic sites. In addition, the calculations of electrostatic interaction energies by using the Buckingham summation method[74] *via* MoProViewer[75] provide information about the co-crystal stability. In the literature, several examples are available which explain not only the binding mechanism of small organic molecular systems but also the protein–ligand complexes by calculating electrostatic parameters.[38,76–80] Therefore, in order to understand the binding mechanism and to compare the stability of both the co-crystals, the calculations of electrostatic potential and electrostatic interaction energies were undertaken by using the following equations

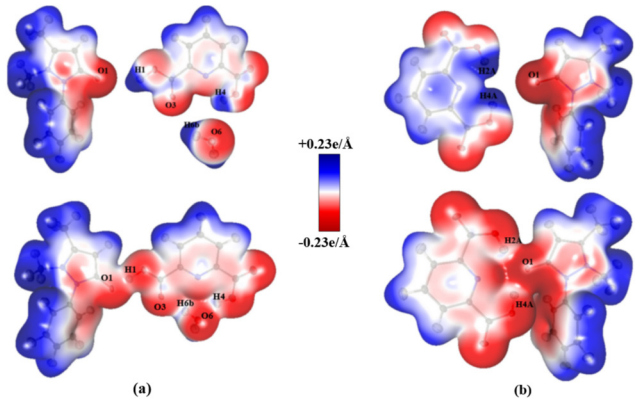

Fig. 5 A three-dimensional electron density surface colored according to the electrostatic potential at the 0.05 e Å^{-3} contour level of the individual fragments (upper) and the asymmetric units (lower): (a) **ANT–DPA-w** and (b) **ANT–DPA**.

$$V(r) = \sum_A \frac{Z_A}{|R_{A-r}|} - \int \frac{\rho(\acute{r})}{|\acute{r} - r|} d\acute{r}$$

$$E^{A,B} = \int \rho^A(\vec{r}) V^B(\vec{r}) d(\vec{r})$$

Fig. 5 illustrates the 3D electron density surface of both the cocrystals coloured according to the electrostatic potential they generate. These calculations use electron densities calculated from the theoretical structure factors employing the experimental coordinates. In both the cocrystals, the ANT moiety has negative potential concentrated on the O1 oxygen atom but it is also spread in its vicinity. However, in the case of DPA, the negative potential is spread over a wider region. Both the carboxylic groups are in the vicinity of negative potential and positive potential is observed on the hydrogen atoms attached to the O2 and O4 atoms of DPA. In the case of **ANT–DPA-w**, the potential of the dicarboxylic acid of DPA is complemented by the opposing potential of a water molecule. Evidently, the electrostatic attraction between the water molecule and the dicarboxylic part of the DPA is stronger than that between the dicarboxylic region and the carbonyl part of the antipyrine. The dicarboxylic part of the DPA is locked by the water molecule. The negative potential on the O1 atom of ANT and the positive potential on the H1 atom of DPA result in a strong hydrogen bond between **ANT–DPA**. However, in the absence of a water molecule in **ANT–DPA**, the dicarboxylic group of DPA is free to interact with the O1 oxygen atom of ANT thus resulting in a different arrangement.

Table 5 lists the electrostatic interaction energies between the dimers of both the co-crystals. Although O···H–O classical hydrogen bonds are possessed by both the cocrystals, the highest interaction energy exists between the **water–DPA** dimer in **ANT–DPA-w** which is close to −398.5 kJ mol^{-1}. **ANT–DPA-w** is also superior in terms of **DPA–ANT** dimer energy (−327.3 kJ mol^{-1}), while the same dimer in **ANT–DPA** has a lower interaction energy (−180.3 kJ mol^{-1}). From these values, it becomes evident that the cocrystallization starts with the formation of a dimer between water and dipicolinic acid which further connects with antipyrine. The presence of water dictates the orientation of the coformers thus resulting in more stable **ANT–DPA-w**. However, **ANT–DPA** which is next in hierarchy is obtained under anhydrous conditions. Table 5 also reveals the role of some other weak interactions such as C–H···C and C–H···O in the stability of both the cocrystals.

Conclusion

In the present study, we have reported two new cocrystal phases of the antipyrine–dipicolinic acid system, one of which is a 'disappearing' phase. The hydrated phase was

Table 5 The electrostatic interaction energies of both cocrystals of **ANT–DPA** calculated based on multipolar refinement using theoretical structure factors

Interactions in the hydrated form		Electrostatic interaction energies (kJ mol^{-1}) in the hydrated form	Interactions in the anhydrous form		Electrostatic interaction energies (kJ mol^{-1}) in the anhydrous form
O2–H1···O1	**DPA–ANT**	−327.3	O4–H4A···O1	**DPA–ANT**	−180.3
O4–H4···O6	**Water–DPA**	*−398.5*	O2–H2A···O1		*−125.2*
O6–H6b···O3					
O6–H6a···O3^{iv}	**Water–DPA**	−39.20	C6–H6···O5^{v}	**ANT–DPA**	−46.61
		−35.40			*−29.74*
C6–H6···C14^{vi}	**ANT–DPA**	−25.80	C2–H2···O5^{iii}	**ANT–DPA**	−44.66
		−28.38			*−34.32*
C4–H4a···O5^{i}	**ANT–DPA**	−23.66	C11–H11C···O3^{iv}	**ANT–DPA**	−25.39
		−18.06			*−14.90*
C10–H10c···C5^{ii}	**ANT–ANT**	−16.32	C14–H14···O3^{ii}	**DPA–DPA**	−19.24
		−5.431			*−9.400*
C15–H15···C3^{iii}	**DPA–ANT**	−14.41	C11–H11B···O1^{v}	**ANT–ANT**	−10.15
		−12.39			*−9.684*
C3–H3···O6^{v}	**ANT–water**	−9.847	C15–H15···C11^{i}	**DPA–ANT**	0.192
		−5.711			*−3.324*

Symmetry codes **ANT–DPA-w:** (i) $x - 1/2, -y + 1/2, z - 1/2$; (ii) $x, y + 1, z$; (iii) $x + 1/2, -y + 3/2, z + 1/2$; (iv) $-x + 3/2, -y + 1/2, -z + 1$; (v) $-x + 1, -y + 1, -z + 1$; (vi) $-x + 3/2, -y + 3/2, -z + 1$. Symmetry codes **ANT–DPA:** (i) $x, y - 1, z$; (ii) $-x + 1/2, y - 1/2, z$; (iii) $x, y + 1/2, z - 1/2$; (iv) $-x + 1/2, y + 1/2, z$; (v) $x, y + 1/2, z + 1/2$.

stable and easily reproducible while the anhydrous phase was serendipitously observed in the same vial as a weak crystal. Analyses of crystal structures revealed that both the cocrystals (**ANT–DPA-w** and **ANT–DPA**) significantly differed in their conformations. Repeated trials under different conditions produced only the hydrated phase. Thermal analysis and the calculation of enthalpy of dehydration (15 kcal mol^{-1}) showed that the hydrated phase is thermally more stable. Computational studies involving SAPT0 analysis, NCI analysis and binding energies showed that additional stabilization energy ~19 kcal mol^{-1}, which lies in close agreement with the experimentally measured enthalpy of dehydration, is provided by the water molecule, thus making the hydrated form the predominant one. The hydrated phase provides more abundant sites for hydrogen bonding and helps in charge stabilization over a wider region. It was inferred from the thermal and computational analyses that the anhydrous phase (**ANT–DPA**) might be regained if an anhydrous environment is provided which was done by melting the hydrated phase and instantly pouring a non-aqueous solvent which upon evaporation gave good quality crystals of anhydrous **ANT–DPA**. The electrostatic interaction energies showed that the water molecule dictates the onset of cocrystallization which starts with the formation of a dimer between dipicolinic acid and water which further connects to an antipyrine moiety. The dimer energies indicate that an anhydrous phase, being next in hierarchy, should be obtained if water is removed. Topological analysis showed that the O–H···O hydrogen bonds are stronger with higher values of electron density on the critical points in the hydrated phase (**ANT–DPA-w**), which makes it more stable than the anhydrous one. The current study emphasizes the significance of using thermal profiling at the early stages of characterization of multi-component drugs as it can pave the way for the discovery of new crystalline forms. The use of computational and charge density methods including SAPT0 and NCI analyses as well as analyses of topological and electrostatic properties can successfully complement the thermal analysis to investigate the relative stability of different crystalline forms, especially pseudopolymorphs.

Conflicts of interest

All the authors declare no conflict of interests.

Acknowledgements

The authors are grateful to the Higher Education Commission and the Federal Government of Pakistan for funding under the Public Sector Development Programme to establish the Materials Chemistry Laboratory at The Islamia University of Bahawalpur, Pakistan, which made this study possible.

References

1 N. Blagden, M. de Matas, P. T. Gavan and P. York, *Adv. Drug Delivery Rev.*, 2007, **59**(7), 617–630.
2 A. Karagianni, M. Malamatari and K. Kachrimanis, *Pharmaceutics*, 2018, **10**(1), 18–47.
3 G. Kuminek, F. Cao, A. B. D. O. da Rocha, S. G. Cardoso and N. Rodriguez-Hornedo, *Adv. Drug Delivery Rev.*, 2016, **101**, 143–166.
4 S. Aitipamula, R. Banerjee, A. K. Bansal, K. Biradha, M. L. Cheney, A. R. Choudhury and M. J. Zaworotko, *Cryst. Growth Des.*, 2012, **12**(5), 2147–2152.
5 C. B. Aakeröy and P. B. Hitchcock, *J. Mater. Chem.*, 1993, **3**(11), 1129–1135.
6 S. Tothadi and G. R. Desiraju, *Philos. Trans. R. Soc., A*, 2012, **370**(1969), 2900–2915.
7 R. M. Bhardwaj, L. S. Price, S. L. Price, S. M. Reutzel-Edens, G. J. Miller, I. D. Oswald and A. J. Florence, *Cryst. Growth Des.*, 2013, **13**(4), 1602–1617.
8 R. Dubey, M. S. Pavan, T. N. Guru Row and G. R. Desiraju, *IUCrJ*, 2014, **1**(1), 8–18.
9 R. Kaur, R. Gautam, S. Cherukuvada and T. N. Guru Row, *IUCrJ*, 2015, **2**(3), 341–351.
10 S. Aitipamula, P. S. Chow and R. B. Tan, *CrystEngComm*, 2014, **16**(17), 3451–3465.
11 N. Madusanka, M. D. Eddleston, M. Arhangelskis and W. Jones, *Acta Crystallogr., Sect. B: Struct. Sci., Cryst. Eng. Mater.*, 2014, **70**(1), 72–80.
12 D. Li, J. Li, Z. Deng and H. Zhang, *CrystEngComm*, 2019, **21**(28), 4145–4149.
13 U. J. Griesser, *Polymorphism: In the pharmaceutical industry*, 2006, pp. 211–233.
14 *Crystallization: basic concepts and industrial applications*, ed. W. Beckmann, John Wiley & Sons, 2013.
15 E. Brini, C. J. Fennell, M. Fernandez-Serra, B. Hribar-Lee, M. Luksic and K. A. Dill, *Chem. Rev.*, 2017, **117**(19), 12385–12414.
16 M. D. Ticehurst, R. A. Storey and C. Watt, *Int. J. Pharm.*, 2002, **247**(1–2), 1–10.
17 L. F. Huang and W. Q. T. Tong, *Adv. Drug Delivery Rev.*, 2004, **56**(3), 321–334.
18 I. Sathisaran and S. V. Dalvi, *Pharmaceutics*, 2018, **10**(3), 108–181.
19 E. Jurczak, A. H. Mazurek, L. Szeleszczuk, D. M. Pisklak and M. Zielińska-Pisklak, *Pharmaceutics*, 2020, **12**(10), 959–983.
20 C. Ahlneck and G. Zografi, *Int. J. Pharm.*, 1990, **62**(2–3), 87–95.
21 D. E. Braun, T. Gelbrich, V. Kahlenberg and U. J. Griesser, *Mol. Pharmaceutics*, 2014, **11**(9), 3145–3163.
22 Y. A. Abramov, *Org. Process Res. Dev.*, 2013, **17**(3), 472–485.
23 E. Shefter and G. Kmack, *J. Pharm. Sci.*, 1967, **56**(8), 1028–1029.
24 E. Shefter and T. Higuchi, *J. Pharm. Sci.*, 1963, **52**(8), 781–791.
25 D. Giron, C. Goldbronn, M. Mutz, S. Pfeffer, P. Piechon and P. Schwab, *J. Therm. Anal. Calorim.*, 2002, **68**(2), 453–465.
26 S. R. Vippagunta, H. G. Brittain and D. J. Grant, *Adv. Drug Delivery Rev.*, 2001, **48**(1), 3–26.
27 N. Blagden, S. J. Coles and D. J. Berry, *CrystEngComm*, 2014, **16**(26), 5753–5761.
28 Q. Tao, J. M. Chen, L. Ma and T. B. Lu, *Cryst. Growth Des.*, 2012, **12**(6), 3144–3152.

29 T. P. Singh and M. Vijayan, *Acta Crystallogr., Sect. B: Struct. Crystallogr. Cryst. Chem.*, 1974, **30**(3), 557–562.
30 L. Olsen, C. Oostenbrink and F. S. Jorgensen, *Adv. Drug Delivery Rev.*, 2015, **86**, 61–71.
31 B. Das and J. B. Baruah, *Cryst. Growth Des.*, 2011, **11**(1), 278–286.
32 A. A. Hindle and E. A. H. Hall, *Analyst*, 1999, **124**, 1599–1604.
33 D. C. Crans, M. Mahroof-Tahir, M. D. Johnson, P. C. Wilkins, L. Yang, K. Robbins and G. R. Willsky, *Inorg. Chim. Acta*, 2003, **356**, 365–378.
34 M. Nakai, H. Watanabe, C. Fujiwara, H. Kakegawa, T. Satoh, J. Takada and H. Sakurai, *Biol. Pharm. Bull.*, 1995, **18**(5), 719–725.
35 H. Sakurai, K. Fujii, S. Fujimoto, Y. Fujisawa, K. Takechi and H. Yasui, *ACS Symp. Ser.*, 1998, **711**, 344.
36 A. Moghimi, H. R. Khavasi, F. Dashtestani, D. Kordestani, E. Behboodi and B. Maddah, *J. Struct. Chem.*, 2013, **54**(5), 990–995.
37 B. Das and J. B. Baruah, *Cryst. Growth Des.*, 2011, **11**(12), 5522–5532.
38 A. Iqbal, A. Mehmood, S. Noureen, C. Lecomte and M. Ahmed, *Acta Crystallogr., Sect. B: Struct. Sci., Cryst. Eng. Mater.*, 2021, **77**(6), 1035–1047.
39 A. Bilal, A. Mehmood, S. Noureen, C. Lecomte and M. Ahmed, *CrystEngComm*, 2022, **24**(44), 7758–7770.
40 R. F. W. Bader, *Atoms in molecules*, Clarendon Press, Oxford, New York, 1994.
41 R. F. W. Bader, *J. Phys. Chem. A*, 1998, **102**, 7314–7323.
42 D. E. Boycov, A. N. Manin, K. V. Drozd, A. V. Churakov and G. L. Perlovich, *CrystEngComm*, 2022, **24**(12), 2280–2290.
43 *Bruker SAINT+, version 6.02 (includes XPREP and SADABS)*, Bruker AXS Inc., Madison, Wisconsin, USA, 1999.
44 O. V. Dolomanov, L. J. Bourhis, R. J. Gildea, J. A. K. Howard and H. Puschmann, *J. Appl. Crystallogr.*, 2009, **42**, 339–341.
45 F. H. Allen and I. J. Bruno, *Acta Crystallogr., Sect. B: Struct. Sci.*, 2010, **66**(3), 380–386.
46 R. Dovesi, A. Erba, R. Orlando, C. M. Zicovich-Wilson, B. Civalleri, L. Maschio and B. Kirtman, *WIREs Comput. Mol. Sci.*, 2018, **8**(4), e1360.
47 J. D. Chai and M. Head-Gordon, *J. Chem. Phys.*, 2008, **128**(8), 084106.
48 D. Vilela Oliveira, J. Laun, M. F. Peintinger and T. Bredow, *J. Comput. Chem.*, 2019, **40**(27), 2364–2376.
49 C. Gatti, V. R. Saunders and C. Roetti, *J. Chem. Phys.*, 1994, **101**, 10686–10696.
50 S. Casassa, A. Erba, J. Baima and R. Orlando, *J. Comput. Chem.*, 2015, **36**, 1940–1946.
51 M. J. Frisch, G. W. Trucks, H. B. Schlegel, G. E. Scuseria, M. A. Robb, J. R. Cheeseman and D. J. Fox, *Gaussian 16 Rev. C. 01*, Wallingford, CT, 2016.
52 Y. Zhao and D. G. Truhlar, *Theor. Chem. Acc.*, 2008, **120**(1), 215–241.
53 T. H. Dunning, *J. Chem. Phys.*, 1989, **90**(2), 1007–1023.
54 S. F. Boys and F. Bernardi, *Mol. Phys.*, 1970, **19**(4), 553–566.
55 E. R. Johnson, S. Keinan, P. Mori-Sánchez, J. Contreras-García, A. J. Cohen and W. Yang, *J. Am. Chem. Soc.*, 2010, **132**(18), 6498–6506.
56 T. Lu and F. Chen, *J. Comput. Chem.*, 2012, **33**(5), 580–592.
57 B. Jeziorski, R. Moszynski and K. Szalewicz, *Chem. Rev.*, 1994, **94**(7), 1887–1930.
58 K. Szalewicz, *WIREs Comput. Mol. Sci.*, 2012, **2**(2), 254–272.
59 D. G. A. Smith, L. A. Burns, A. C. Simmonett, R. M. Parrish, M. C. Schieber, R. Galvelis, P. Kraus, H. Kruse, R. Di Remigio, A. Alenaizan and A. M. James, *J. Chem. Phys.*, 2020, **152**(18), 184108.
60 J. J. McKinnon, F. P. Fabbiani and M. A. Spackman, *Cryst. Growth Des.*, 2007, **7**(4), 755–769.
61 M. A. Spackman and D. Jayatilaka, *CrystEngComm*, 2009, **11**(1), 19–32.
62 M. J. Turner, J. J. McKinnon, S. K. Wolff, D. J. Grimwood, P. R. Spackman, D. Jayatilaka and M. A. Spackman, *CrystalExplorer17*, University of Western Australia, 2017.
63 J. Van de Streek and M. A. Neumann, *Acta Crystallogr., Sect. B: Struct. Sci.*, 2010, **6**(5), 544–558.
64 M. Stein and M. Heimsaat, *Crystals*, 2019, **9**(12), 665.
65 E. R. Johnson, S. Keinan, P. Mori-Sánchez, J. Contreras-García, A. J. Cohen and W. Yang, *J. Am. Chem. Soc.*, 2010, **132**(18), 6498–6506.
66 U. Koch and P. L. Popelier, *J. Phys. Chem.*, 1995, **99**(24), 9747–9754.
67 J. S. Murray and P. Politzer, *Wiley Interdiscip. Rev.: Comput. Mol. Sci.*, 2011, **1**(2), 153–163.
68 N. Zhu, C. L. Klein Stevens and E. D. Stevens, *J. Chem. Crystallogr.*, 2005, **35**, 13–22.
69 D. S. Arputharaj, V. R. Hathwar, T. N. Guru Row and P. Kumaradhas, *Cryst. Growth Des.*, 2012, **12**(9), 4357–4366.
70 C. Kalaiarasi, M. S. Pavan and P. Kumaradhas, *Acta Crystallogr., Sect. B: Struct. Sci., Cryst. Eng. Mater.*, 2016, **72**(5), 775–786.
71 G. Rajalakshmi, V. R. Hathwar and P. Kumaradhas, *Acta Crystallogr., Sect. B: Struct. Sci., Cryst. Eng. Mater.*, 2014, **70**(3), 568–579.
72 G. Rajalakshmi, V. R. Hathwar and P. Kumaradhas, *Acta Crystallogr., Sect. B: Struct. Sci., Cryst. Eng. Mater.*, 2014, **70**(2), 331–341.
73 E. J. Yearley, E. A. Zhurova, V. V. Zhurov and A. A. Pinkerton, *J. Am. Chem. Soc.*, 2007, **129**(48), 15013–15021.
74 A. D. Buckingham, *Adv. Chem. Phys.*, 1967, **12**, 107–142.
75 B. Guillot, *Acta Crystallogr., Sect. A: Found. Crystallogr.*, 2012, **68**, 204.
76 S. Swaminathan, B. M. Craven, M. A. Spackman and R. F. Stewart, *Acta Crystallogr., Sect. B: Struct. Sci.*, 1984, **40**(4), 398–404.
77 M. A. Spackman, H. P. Weber and B. M. Craven, *J. Am. Chem. Soc.*, 1988, **110**(3), 775–782.
78 N. Bouhmaida, N. E. Ghermani, C. Lecomte and A. Thalal, *Acta Crystallogr., Sect. A: Found. Crystallogr.*, 1997, **53**(5), 556–563.
79 N. Muzet, B. Guillot, C. Jelsch, E. Howard and C. Lecomte, *Proc. Natl. Acad. Sci. U. S. A.*, 2003, **100**(15), 8742–8747.
80 A. Volkov and P. Coppens, *Comput. Chem.*, 2004, **25**(7), 921–934.

